3-14-2017

Simultaneous upward and downward propagating inertia-gravity waves in the MLT observed at Andes Lidar Observatory

Kai Ming Hung
Wuhan University, University of Science and Technology of China, State Observatory for Atmospheric Remote Sensing

Alan Z. Liu
Embry-Riddle Aeronautical University

Shao Dong Zhang
Wuhan University, State Observatory for Atmospheric Remote Sensing

Fan Yi
Wuhan University, State Observatory for Atmospheric Remote Sensing

Chun Ming Huang
Wuhan University, State Observatory for Atmospheric Remote Sensing

See next page for additional authors

Scholarly Commons Citation

Huang, K. M., A. Z. Liu, S. D. Zhang, F. Yi,C. M. Huang, Y. Gong, Q. Gan, Y. H.Zhang, and R. Wang (2017),Simultaneous upward and downward propagating inertia-gravity waves in theMLT observed at Andes Lidar Observatory, J. Geophys. Res. Atmos.,122, 2812–2830, doi:10.1002/2016JD026178.

AGU PUBLICATIONS

JGR

Journal of Geophysical Research: Atmospheres

RESEARCH ARTICLE
10.1002/2016JD026178

Key Points:
- Upward and downward propagating IGWs are simultaneously observed by lidar, and downward propagating IGWs in the MLT were rarely reported ago
- Instability arising from multiple wave superposition has a significant influence on wave saturation and amplitude constraint
- Upward a propagating IGW probably originates from polar jet adjustment, while downward propagating IGW source region may be above the MLT

Correspondence to:
S. D. Zhang,
zsd@whu.edu.cn

Citation:
Huang, K. M., A. Z. Liu, S. D. Zhang, F. Yi, C. M. Huang, Y. Gong, Q. Gan, Y. H. Zhang, and R. Wang (2017), Simultaneous upward and downward propagating inertia-gravity waves in the MLT observed at Andes Lidar Observatory, *J. Geophys. Res. Atmos.*, *122*, 2812–2830, doi:10.1002/2016JD026178.

Received 24 NOV 2016
Accepted 28 FEB 2017
Accepted article online 6 MAR 2017
Published online 14 MAR 2017

Simultaneous upward and downward propagating inertia-gravity waves in the MLT observed at Andes Lidar Observatory

Kai Ming Huang[1,2,3], Alan Z. Liu[4], Shao Dong Zhang[1,3], Fan Yi[1,3], Chun Ming Huang[1,3], Yun Gong[1,3], Quan Gan[1,3], Ye Hui Zhang[5], and Rui Wang[6]

[1]School of Electronic Information, Wuhan University, Wuhan, China, [2]Key Laboratory of Geospace Environment, Chinese Academy of Sciences, University of Science and Technology of China, Hefei, China, [3]State Observatory for Atmospheric Remote Sensing, Wuhan, China, [4]Department of Physical Science, Embry-Riddle Aeronautical University, Daytona Beach, Florida, USA, [5]College of Hydrometeorology, Nanjing University of Information Science and Technology, Nanjing, China, [6]SOA Key Laboratory for Polar Science, Polar Research Institute of China, Shanghai, China

Abstract Based on the temperature and zonal and meridional winds observed with an Na lidar at Andes Lidar Observatory (30.3°S, 70.7°W) on the night of 20–21 July 2015, we report simultaneous upward and downward propagating inertia-gravity waves (IGWs) in the mesosphere/lower stratosphere (MLT). The ground-based periods of the upward and downward IGWs are about 5.4 h and 4.8 h, respectively. The horizontal and vertical wavelengths are about 935 km and 10.9 km for the 5.4 h IGW and about 1248 km and 22 km for the 4.8 h IGW, respectively. Hodograph analyses indicate that the 5.4 h IGW propagates in the direction of about 23° west of north, while the 4.8 h IGW travels northward with an azimuth of 20°clockwise from north. These wave parameters are in the typical IGW wavelength and period ranges; nevertheless, the downward propagating IGWs in the MLT are rarely reported in previous observations. The ray-tracing analysis suggests that the 5.4 h IGW is likely to originate from the stratospheric jet adjustment over the Antarctic, while the 4.8 h IGW source may be above the MLT because it is unlikely to propagate downward through a reflection in the realistic atmospheric wind field. Although both IGWs do not reach their amplitude thresholds of instability, the Richard number reveals that the dynamical and convective instabilities occur intermittently, which indicates that the instability arising from the multiple-perturbation superposition may have a significant influence on wave saturation and amplitude constraint in the MLT.

1. Introduction

Gravity waves (GWs) play an important role in determining large-scale circulations, thermal states, and dynamics of the middle and upper atmosphere because of their inherent ability to transport momentum and energy among different atmospheric layers [*Lindzen*, 1981]. As medium- and small-scale perturbations, GWs can be excited through many dynamical and thermodynamical processes in the atmosphere. Convection, wind shear instability, flow over topography, and geostrophic adjustment are generally regarded as the dominant sources of GWs in the lower atmosphere [*Fritts and Alexander*, 2003], and additional sources, such as body forcing accompanying localized wave dissipation [*Fritts et al.*, 2002; *Vadas et al.*, 2003], auroral heating [*Sofko and Huang*, 2000], and wave-wave interaction [*Huang et al.*, 2009, 2013], are of significance in the middle and upper atmosphere. Convection can excite broad spectrum range GWs [*Yuan et al.*, 2016]. GWs originating from unstable shear flow have typical horizontal wavelengths of a few to tens of kilometers with horizontal phase speeds comparable to the mean wind. GWs associated with topography have various wavelengths depending on topographic scales [*Pautet et al.*, 2016], and flow over large mountain can generate mesoscale inertia-gravity waves (IGWs) propagating opposite to the background flow with ground-based horizontal phase speeds near zero. Geostrophic adjustment radiates waves characterized by IGWs, which has horizontal wavelengths of hundreds to thousands of kilometers and periods of hours up to the inertial period.

IGWs influenced by the Earth rotation are primary mesoscale atmospheric wave. Model studies have demonstrated that the realistic quasi-biennial and semiannual oscillations in the stratosphere and mesosphere cannot be simulated properly without parameterized IGW fluxes [*Dunkerton*, 1997; *Sassi and Garcia*, 1997]. IGW signatures frequently appear in the atmospheric temperature and wind fields. In the troposphere and

lower stratosphere (TLS), a great number of studies investigated not only IGW cases but also statistical distributions of horizontal and vertical wavelengths, period, propagation direction, kinetic and potential energies, and momentum flux of IGWs and their seasonal and interannual variations in different latitudes based on radar and lidar observations [*Cho*, 1995; *Riggin et al.*, 1995, 1997; *Sato et al.*, 1997; *Wilde et al.*, 1997; *Nastrom and Eaton*, 2006; *Kumar and Ramkumar*, 2008; *Ratnam et al.*, 2008], rocket sounding [*Hamilton*, 1991; *Eckermann et al.*, 1994], and radiosonde observations [*Tsuda et al.*, 1994; *Shimizu and Tsuda*, 1997; *Pfenninger et al.*, 1999; *Vincent and Alexander*, 2000; *Zink and Vincent*, 2001; *Yoshiki et al.*, 2004; *Zhang and Yi*, 2005, 2007; *Yamamori and Sato*, 2006; *Vincent et al.*, 2007; *Ki and Chun*, 2011; *Moffat-Griffin et al.*, 2013; *Murphy et al.*, 2014]. These observations suggested that IGWs in the TLS have typical horizontal wavelengths of 200–2000 km, vertical wavelengths of 2–10 km, and intrinsic frequencies of 2–5 *f* (where *f* is the inertial frequency). In the upper stratosphere and mesosphere/lower thermosphere (MLT), IGWs were reported from lidar [*Collins et al.*, 1994; *Hu et al.*, 2002; *Rajeev et al.*, 2003; *Xu et al.*, 2006; *Li et al.*, 2007, 2010; *Lu et al.*, 2009, 2015a, 2015b, 2017; *Chen et al.*, 2013, 2016; *Cai et al.*, 2014; *Baumgarten et al.*, 2015] and radar [*Muraoka et al.*, 1987; *Yamamoto et al.*, 1987; *Gavrilov et al.*, 2000; *Zhou and Morton*, 2006; *Nicolls et al.*, 2010; *Chen et al.*, 2011, 2014, 2015; *Suzuki et al.*, 2013] measurements. These observations indicate that most IGWs in the MLT evidently exhibited a quasi-monochromatic feature. Relative to extensive investigations of lower atmospheric IGWs in different latitudes and seasons, observational studies of IGWs in the MLT are not sufficient to fully understand the features of their activities in the MLT.

Based on profiles of wind and temperature from radiosonde and radar, hodograph technique derived from the IGW polarization relation is used to determine propagation direction and intrinsic frequency [*Holton*, 2004]. Hodograph method is viewed as an accurate technique when a monochromatic IGW with large amplitude propagates in a background field which has weak shear and slow temporal variation. Modeling study [*Zhang et al.*, 2004] showed that there is a large uncertainty for intrinsic frequency derived from individual profiles by using hodograph technique, which leads to large error in estimate of horizontal wavelength. Similarly, observational analysis [*Chen et al.*, 2013] also found that the ratio of fitted hodographic ellipse major to minor axis varies dramatically with altitude due to the background atmospheric variation and other spectral component influences. However, the direction of major axis is relatively consistent, suggesting that it is reliable for estimating horizontal propagation direction. Once horizontal propagation direction is determined, intrinsic frequency and horizontal wavelength can be reliably estimated by means of combining the IGW polarization relation with the Doppler shift equation [*Li et al.*, 2007; *Chen et al.*, 2013]. In this study, we investigate IGW activities observed by a narrowband Na wind and temperature lidar at Andes Lidar Observatory (ALO) in Cerro Pachón, Chile (30.3°S, 70.7°W) by using hodograph method. In particular, a downward propagating IGW in the MLT will be presented, which is helpful in understanding the characteristics of IGWs in the MLT.

In the next section, the recent Na lidar at ALO and observational data are briefly described. In section 3, upward and downward propagating IGWs observed by lidar are analyzed, and their wavelengths, propagation directions, and intrinsic periods are estimated. In section 4, possible sources and instabilities of IGWs are discussed. A summary is given in section 5.

2. Lidar Data

The lidar-measured neutral atmospheric wind and temperature over a period of 10.7 h from 2330 UT, 20 July 2015, are used to investigate the GW activities. The Na lidar system has about 0.4–0.6 W m^2 power aperture product and was upgraded in May 2014 by using a high-power amplified diode laser as the master oscillator, and the receiver was improved with more efficient coupling from the telescope to the photomultiplier tube [*Smith and Chu*, 2015]. The ALO Na lidar upgrade was described in more detail in *Liu et al.* [2016]. The lidar measures the wind and temperature by using the three-frequency technique [*She and Yu*, 1994]. The laser is locked sequentially at the Na resonance frequency at the D2a line, and the two frequencies shifted by ±630 MHz. The temperature and line-of-sight wind are derived based on the ratios among the backscattered signals at these three frequencies [*Krueger et al.*, 2015]. The Na density, line-of-sight wind, temperature profiles in zenith, and 20° off-zenith to south and east are measured in sequence with 60 s integration time at each direction on this night. The horizontal winds were calculated by using off-zenith line-of-sight winds. The wind and temperature errors with the three-frequency technique are dominated by photon noise. The

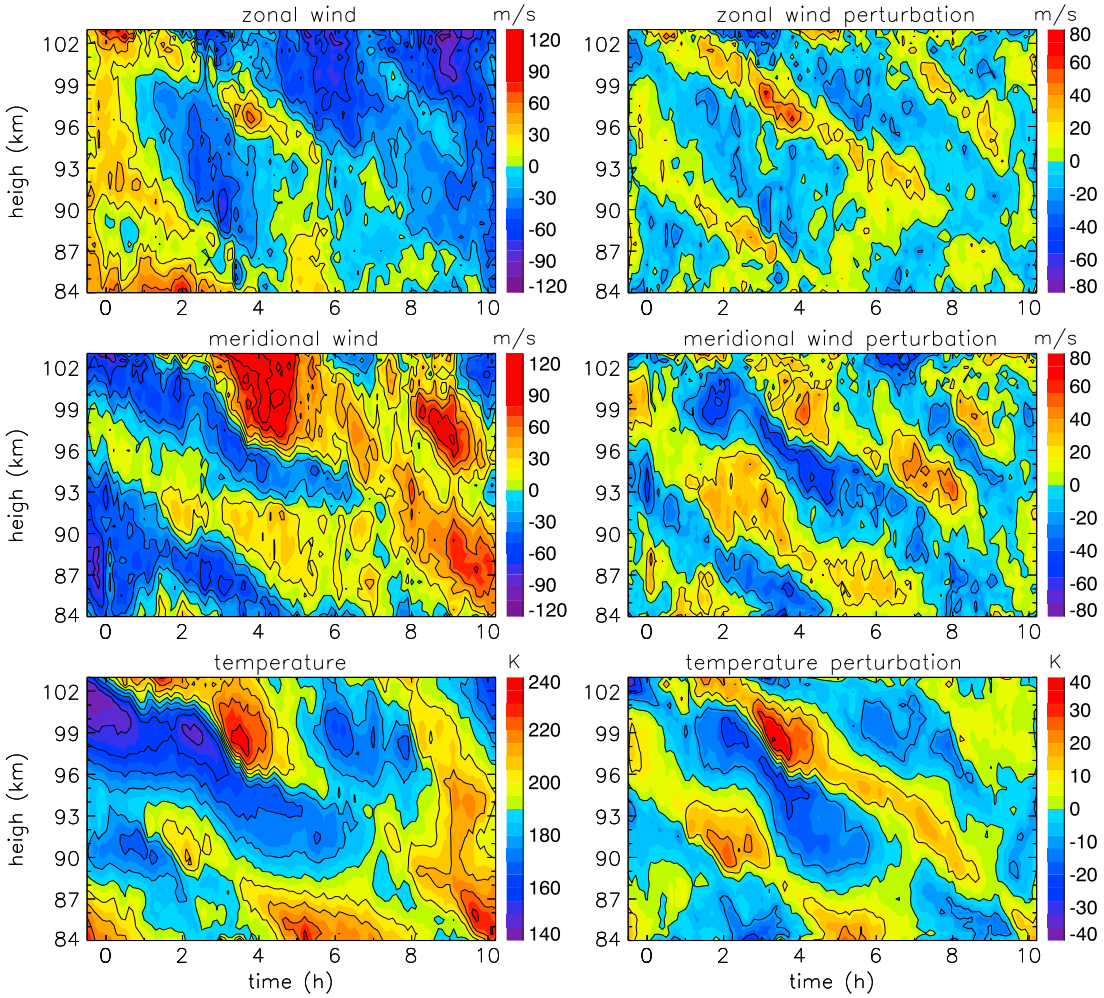

Figure 1. (left column) Lidar observational (top) zonal wind, (middle) meridional wind, and (bottom) temperature at the height of 84–103 km for 10.7 h from 2330 UT, 20 July 2015 and (right column) perturbations of (top) zonal wind, (middle) meridional wind, and (bottom) temperature.

temperature and wind were derived at 500 m, 1 min resolutions, and then smoothed with 1 km, 15 min full-width hamming windows, resulting in effective resolutions of about 0.5 km and 6 min. At this temporal and spatial resolution, the temperature uncertainty is the minimum at 92 km of about 0.5 K and increases to about 1.5 K at 84 km and about 3.0 K at 103 km on this night. The uncertainties of the zonal and meridional winds are estimated to be about 2 ms^{-1} and 1.8 ms^{-1} at 92 km, about 4 ms^{-1} and 3.5 ms^{-1} at 84 km, and about 10 ms^{-1} and 8 ms^{-1} at 103 km, respectively. Only data between 84 km and 103 km are used in the study because the uncertainties increase quickly beyond this range.

3. IGW Perturbations

3.1. Observations and Perturbations

The zonal (positive eastward) and meridional (positive northward) winds and temperature observed by the Na lidar at ALO are shown in Figure 1. The wind and temperature fields exhibit temporal and spatial variabilities, and downward phase progression of the zonal wind, meridional wind, and temperature perturbations can be clearly seen. We use a second-order polynomial fit at each height, and then remove the fitted values to obtain the total wave perturbations, which are also presented in Figure 1. A two-dimensional discrete Fourier transform (DFT) on the total perturbations in the zonal wind, meridional wind, and temperature is used to obtain their frequency-wave number spectra, which are then normalized by

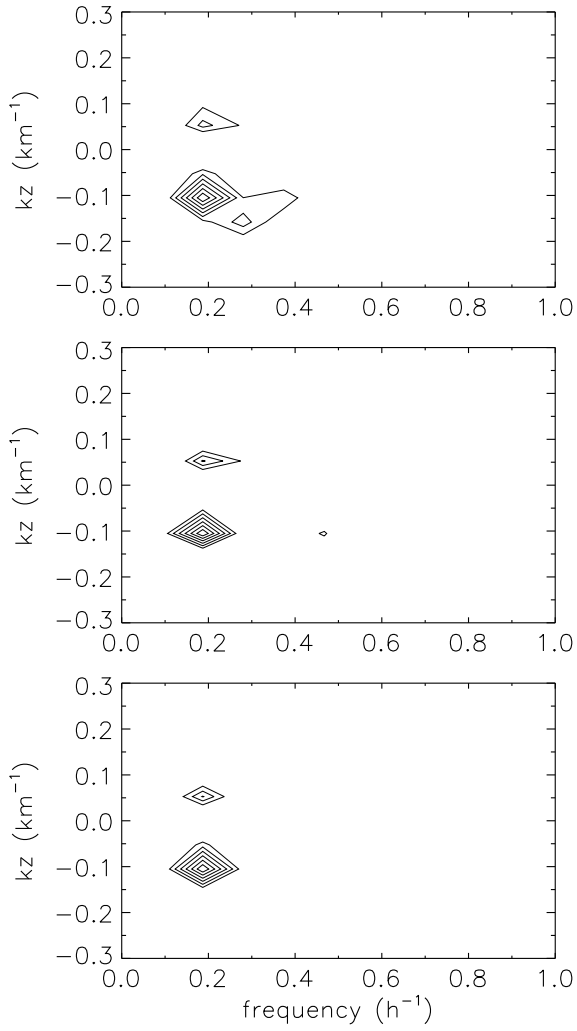

Figure 2. Normalized frequency-wave number spectra of (top) zonal wind, (middle) meridional wind, and (bottom) temperature perturbations derived from DFT. The contour value is from 0.4 to 0.9 with an interval of 0.1.

their maximum spectral magnitudes, as shown in Figure 2. In Figure 2, the frequency and wave number, in units of h^{-1} and km^{-1}, are denoted by the inverses of period and wavelength, respectively. The positive and negative vertical wave numbers represent the upward and downward phase progressions, respectively. There are two spectral peaks at the same frequency corresponding to a period of about 5.4 h that exist in all three fields, and their corresponding vertical wavelengths are 9.5 km and 19 km, respectively. The stronger wave with negative vertical wave number is an upward propagating wave because the vertical direction of the group velocity for GWs is opposite to that of the phase speed. The other relatively weaker wave has positive vertical wave number; thus, it propagates downward. Of course, if we decrease the minimum contour value, then a large number of other spectral components will emerge in Figure 2, which also means that relative to these two IGWs, the remaining fluctuations after subtraction of the background and the two waves from original observations are rather weak. Hence, Figure 2 suggests that there were upward and downward propagating IGWs with large amplitudes simultaneously appearing in the MLT region.

3.2. The Upward Propagating IGW

The above preliminary analysis has limited spectral resolution due to the limited observational time span and height range. To obtain more accurate wave parameters, we separate the upward and downward perturbations by using a two-dimensional filter which includes all spectral components of positive or negative wave numbers, and then a Lomb-Scargle spectrum analysis [*Scargle*, 1982] is performed on the extracted perturbations. The Lomb-Scargle spectrum analysis adopts a 4 time oversampling, corresponding to an effective frequency resolution of 1/42.8 h^{-1} or a wave number resolution of 1/76 km^{-1}. Figure 3 shows the upward propagating perturbations derived from the filtering. It is clear that an IGW dominates the perturbation field. Figure 4 gives the Lomb-Scargle frequency spectra of the upward propagating perturbations in the zonal wind, meridional wind, and temperature at the heights of 84–103 km, and Figure 5 presents their Lomb-Scargle vertical wave number spectra during the observational period. Figures 4 and 5 illustrate that the predominant IGW has a period of 5.4 h, equal to that derived from the DFT, and a vertical wavelength of 10.9 km, slightly larger than that derived from the DFT.

For high-frequency GWs, the horizontal wind perturbation in the direction of wave propagation, $\hat{u}$, tends to be much larger than the perturbation velocity perpendicular to the direction of wave propagation, $\hat{v}$. For IGWs, as the intrinsic frequency decreases toward the inertia frequency, $\hat{v}$ increases and becomes

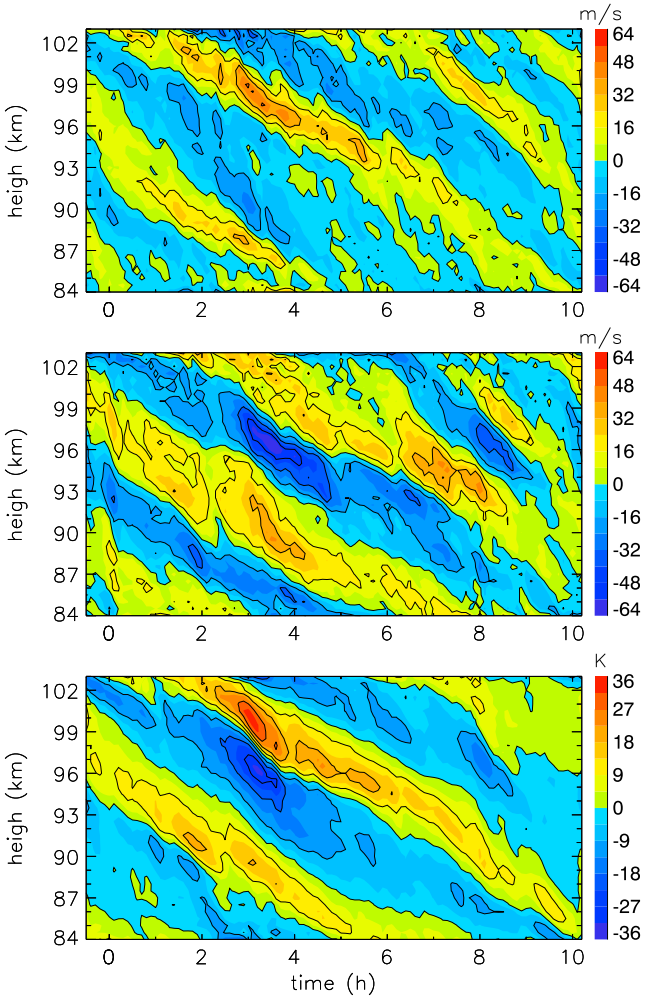

Figure 3. Upward propagating waves in (top) zonal wind, (middle) meridional wind, and (bottom) temperature.

comparable to $\hat{u}$. They obey the polarization relation derived from the linear wave theory as follows [*Tsuda et al.*, 1994; *Fritts and Alexander*, 2003]:

$$\frac{\hat{u}}{\hat{v}} = i\frac{\Omega}{f} \tag{1}$$

where i is the imaginary unit, indicating a 90° phase difference; Ω is the intrinsic frequency; and the inertia frequency $f = -7.4\times10^{-5}\,\mathrm{rad\,s^{-1}}$ at 30.3°S. In the southern hemisphere, $\hat{v}$ leads $\hat{u}$ by 90° due to $f<0$; hence, for upward propagating IGWs with negative vertical wave number ($k_z<0$), the hodograph of the ($\hat{u}$, $\hat{v}$) vector rotates counterclockwise with increasing height or time and forms an ellipse. The direction of wave propagation is along the major axis of the ellipse with a 180° ambiguity. This ambiguity can be removed based on the polarization relation of the horizontal velocity component $\hat{u}$ and the temperature perturbation $\hat{T}$, which is expressed as [*Hu et al.*, 2002; *Li et al.*, 2007]

$$\frac{\hat{T}}{\hat{u}} = \frac{H(ik_z + 1/2H)\left(\Omega^2 - f^2\right)}{R\Omega k_h} \tag{2}$$

where k_h is the horizontal wave number, H is the scale height, and R is the atmospheric gas constant. We can assume a positive direction of k_h from the two directions along the major axis of the hodographic ellipse; thus, the horizontal wind perturbation $\hat{u}$ can be calculated by projecting the zonal and meridional wind perturbations to the assumed propagation direction. According to equation (2), for upward propagating IGWs with $k_z<0$, $\hat{u}$ leads to $\hat{T}$. Thereby, if the hodograph of the ($\hat{u}$, $\hat{T}$) vector rotates clockwise with increasing height or time, then the direction of wave propagation is consistent with the assumed direction; otherwise, the propagation direction is opposite to the assumed direction. Similarly, for downward propagating waves ($k_z>0$) in the southern hemisphere, the hodograph of the ($\hat{u}$, $\hat{v}$) vector rotates clockwise with increasing height or counterclockwise with time. At this time, when the hodograph of the ($\hat{u}$, $\hat{T}$) vector also rotates clockwise with height or counterclockwise with time, the wave propagates along the assumed positive direction. Otherwise, the wave propagates in the opposite direction. Therefore, the direction of horizontal propagation can be identified from the zonal wind, meridional wind, and temperature observed at a single station through the two hodographs.

As shown in Figure 4, the upward propagating IGW has a dominant period of 5.4 h in the zonal wind, meridional wind, and temperature. We fit a sinusoidal wave with this period at each height to obtain the perturbation components of the zonal wind, meridional wind, and temperature. The fitted maximum amplitudes are about 18.5 $\mathrm{ms^{-1}}$ in the zonal wind at 97 km and 28.5 $\mathrm{ms^{-1}}$ and 15.3 K in the meridional wind and temperature at 96 km, respectively. Figure 6 shows the evolution of the fitted initial phase with height. For these initial phases, we make a linear fitting to their variation with height, and the fitted results are also presented in Figure 6. One can see that the meridional wind perturbation leads to the zonal wind perturbation and the zonal wind perturbation leads to the temperature perturbation. Based on the phase variation with height,

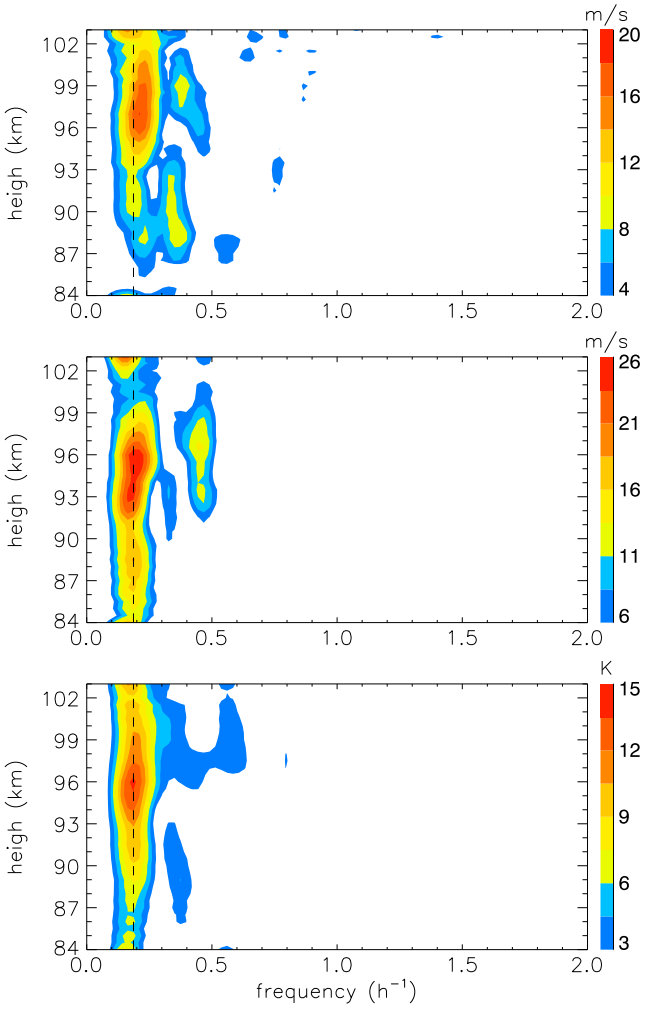

Figure 4. Lomb-Scargle frequency spectra of upward propagating waves in (top) zonal wind, (middle) meridional wind, and (bottom) temperature. The dashed vertical line corresponds to a period of 5.4 h.

we obtain the vertical wavelengths in the zonal wind, meridional wind, and temperature to be 11.1 ± 0.2 km, 10.8 ± 0.3 km, and 11.0 ± 0.2 km, respectively. These values are essentially the same as the 10.9 km derived from the Lomb-Scargle spectrum because their differences are smaller than the vertical resolution of 0.5 km. Thus, the IGW has a vertical wavelength of about 10.9 km.

Figure 7 shows the temporal hodographs of the fitted sin-function zonal and meridional wind perturbation components between 90 and 96 km from the start to the end. The star, square, and triangle represent $t = 0$ h, 1 h, and 2 h, respectively. This height range is chosen because the signal-to-noise ratio is the highest in the range where the Na atom density peak appears and the wave activity is relatively strong. The temporal hodograph is equivalent to the altitudinal hodograph because they have the same theoretical basis [*Chen et al.*, 2013]. As expected, all hodographs exhibit a counterclockwise rotation with time, indicating that the wave propagates upward. Similar to the previous modeling and observational results [*Zhang et al.*, 2004; *Chen et al.*, 2013], we can see from Figure 7 that the ratios of hodographic ellipse major-to-minor axes remarkably change with height, while the directions of major axes exhibit little variability. Hence, the hodograph technique is appropriate to estimate the horizontal propagation direction of the wave but not to derive the intrinsic frequency. Since the wave propagates along the major axis of the hodographic ellipse with a 180° ambiguity, we may assume a positive propagation direction along the major axis, which is denoted by green arrows in Figure 7. The propagation direction is calculated to be 65.9°, 67.4°, 69.7°, and 65.2° south of east at 90 km, 92 km, 94 km, and 96 km, respectively, with an averaged value of 67.1°, which is consistent with the averaged angle of 67.2° over the height range of 84–103 km. In other words, this means that the wave is assumed to propagate at about 157° azimuth. Figure 8 shows the hodographs of the temperature perturbation and the horizontal wind perturbation at 157° azimuth. The counterclockwise rotation of all the four hodographs in Figure 8 indicates that the actual direction is opposite to the assumed direction, at 337° azimuth.

We combine the GW dispersion relation with the Doppler shift equation, instead of equation (1), to calculate the intrinsic frequency and horizontal wavelength for reducing the estimate error. The IGW dispersion relation and Doppler shift equation can be written as follows [*Fritts and Alexander*, 2003; *Liu and Meriwether*, 2004]:

$$k_h^2 = \frac{\Omega^2 - f^2}{N^2}\left(k_z^2 + \frac{1}{4H^2}\right) \tag{3}$$

$$\Omega = \omega - k_h U \tag{4}$$

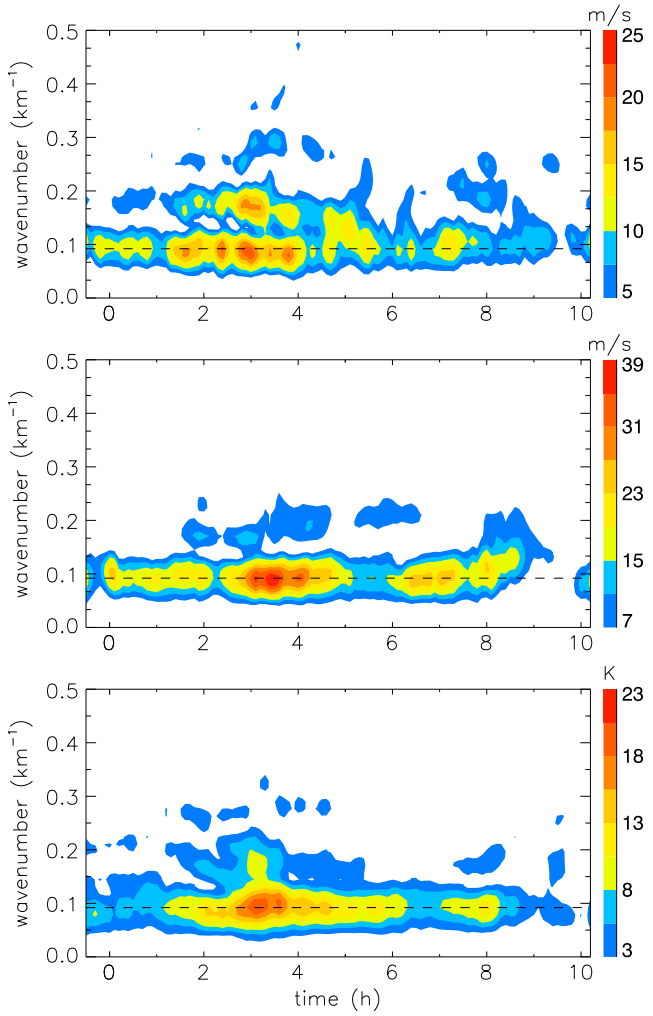

Figure 5. Lomb-Scargle wave number spectra of upward propagating waves in (top) zonal wind, (middle) meridional wind, and (bottom) temperature. The dashed horizontal line corresponds to a wavelength of 10.9 km.

where ω is the ground-based wave frequency, N is the buoyancy frequency, and U is the horizontal background wind velocity determined by projecting the zonal and meridional background winds to the wave propagation direction. It is known that the wave frequency varies with the variational background

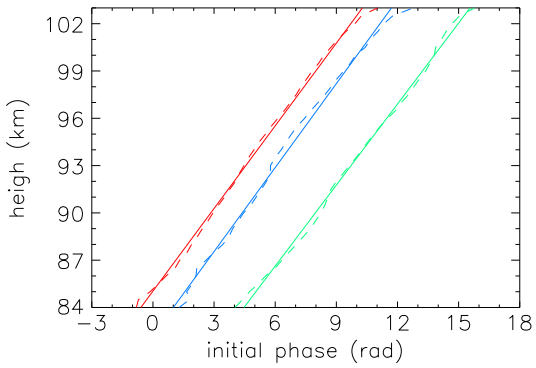

Figure 6. Variation of fitted initial phase with height. The blue, green, and red dashed lines denote the initial phases of the zonal wind, meridional wind, and temperature perturbations of 5.4 h wave derived from sinusoidal wave fitting at each height, respectively, and the blue, green, and red solid lines denote their linearly fitted initial phases, respectively.

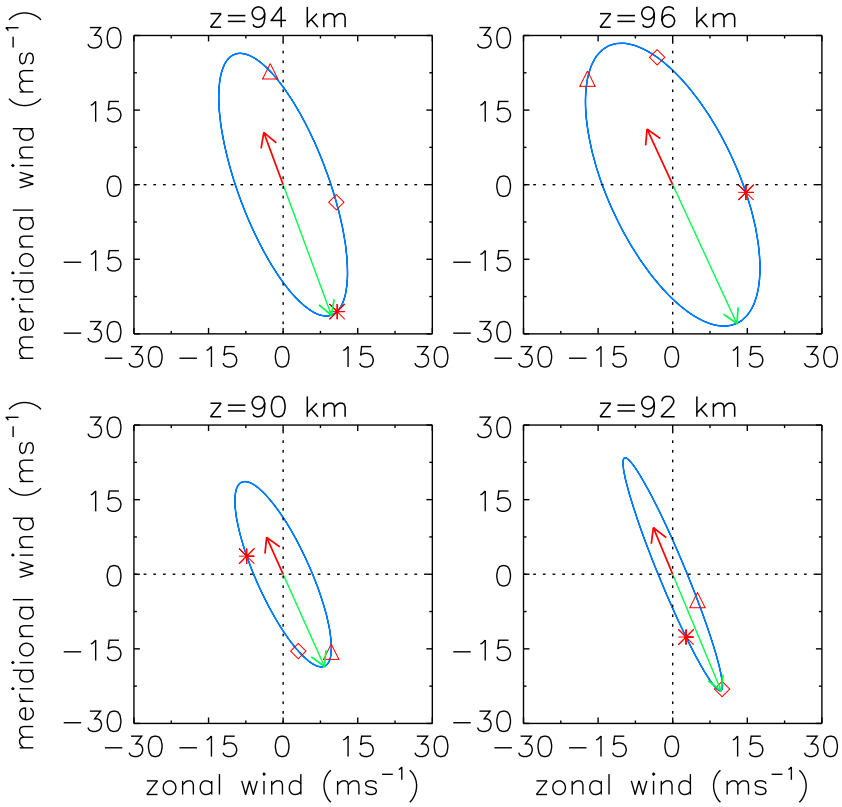

Figure 7. Temporal hodographs of zonal and meridional wind perturbations for 5.4 h wave. The star, square, and triangle are at 0, 1, and 2 h, respectively. The green arrow along the major axis of ellipse denotes the assumed propagation direction of the wave, and the red arrow denotes the realistic propagation direction.

wind [*Yeh and Liu*, 1974; *Huang and Zhang*, 2006]. Since the ground-based frequency and vertical wavelength derived from the spectral analysis are the averaged values over the whole observational time and space domain, here we also neglect the temporal and spatial variabilities of the background fields to roughly estimate the intrinsic frequency and horizontal wavelength based on equations (3) and (4) by using the averaged background wind, buoyancy frequency, and scale height over the whole time and space domain. The zonal wind, meridional wind, and temperature in Figure 1 observed by lidar are averaged to be $-11.3\,\mathrm{ms}^{-1}$, $7.1\,\mathrm{ms}^{-1}$, and 189.5 K, respectively, which are in good agreement with those derived from the fitted background values. The horizontal wind velocity U in the wave propagation direction is calculated to be $10.9\,\mathrm{ms}^{-1}$. The gravitational acceleration is $g = 9.5\,\mathrm{ms}^{-2}$ at about 90 km over 30.3°S; subsequently, the averaged scale height and buoyancy frequency are calculated to be about $H = 5.7$ km and $N = 2.1 \times 10^{-2}\,\mathrm{rad\,s}^{-1}$, respectively. Accordingly, the intrinsic period and horizontal wavelength are about 6.9 h and 935 km derived from equations (3) and (4), respectively, and then, the intrinsic horizontal and vertical group velocities are calculated to be $34.5\,\mathrm{ms}^{-1}$ and $0.4\,\mathrm{ms}^{-1}$, respectively. We can also estimate the intrinsic frequency based on the ratio of horizontal kinetic energy to potential energy of the IGWs [*Geller and Gong*, 2010]. By using the fitted amplitudes, the averaged horizontal kinetic energy and potential energy between 84 km and 103 km are calculated to be $133.2\,\mathrm{Jkg}^{-1}$ and $117.9\,\mathrm{Jkg}^{-1}$, respectively. Thus, the intrinsic period is determined to be 6.7 h, which approximately equals the value of 6.9 h derived from the dispersion relation and Doppler shift equation.

3.3. The Downward Propagating IGW

The downward propagating perturbations extracted by the two-dimensional filtering are shown in Figure 9. Similar to Figure 3, Figure 9 illustrates that a quasi-monochromatic IGW with clearly upward phase progression dominates the perturbation filed. Figures 10 and 11 present the Lomb-Scargle frequency and wave number spectra of the perturbations, respectively. Relative to Figures 4 and 5, it can be seen from

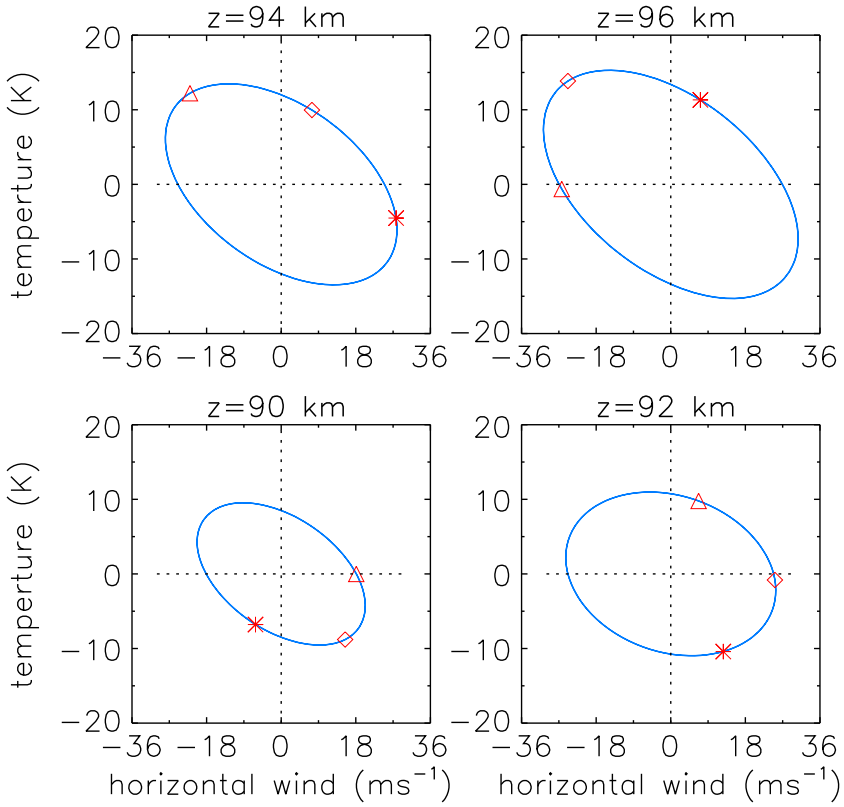

Figure 8. Temporal hodographs of temperature perturbation and horizontal wind perturbation in assumed propagation direction for 5.4 h wave. The star, square, and triangle are at 0, 1, and 2 h, respectively.

Figures 10 and 11 that the dominant frequencies and wave numbers exhibit a slight drift in some height and time, in particular for the zonal wind, which is probably caused by the influence of other spectral components because the downward propagating IGW is a lot weaker than the upward propagating IGW shown in Figure 3 . The Lomb-Scargle spectrum analysis indicates that the ground-based period and vertical wavelength are about 4.8 h and 19 km, respectively. A fitting of sinusoidal wave under a period of 4.8 h on the zonal wind, meridional wind, and temperature perturbations at each height is carried out. The vertical wavelengths in the zonal wind, meridional wind, and temperature are 21.3 km, 22.4 km, and 21.8 km derived from the fitted initial phases, respectively. The wavelength of 19 km resulting from both the DFT and Lomb-Scargle spectrum analyses is slightly smaller than these values because of the limit of spectral resolution. On the basis of the phase variation with height in Figure 9, we can note that the vertical wavelength of the predominant IGW is close to but slightly larger than the observational height range. Therefore, the downward propagating IGW may be considered to have a vertical wavelength of about 22 km.

Figure 12 displays the temporal hodographs of the fitted zonal and meridional wind perturbation components. These counterclockwise rotating hodographs reconfirm the downward propagation feature of the IGW. We choose a positive direction along the major axis of hodograph as the wave propagation direction. The assumed propagation directions denoted by the green arrows in Figure 12 have an averaged azimuth of 19.9° east of north at the four heights, which approximately equal the value of 20.5° averaged over all observational heights. Hence, we can conclude that the wave is propagating at about 20° azimuth. Figure 13 shows the hodographs of the temperature perturbation and the horizontal wind perturbation in this propagation direction. The counterclockwise rotation of the hodographs with time reveals that the horizontal propagation direction agrees with the assumed direction of 20° azimuth. By projecting the zonal and meridional background winds onto this direction, we obtain the horizontal wind velocity $U = 2.8\,\mathrm{ms}^{-1}$ in the direction of propagation. According to equations (3) and (4), the intrinsic period and horizontal wavelength of this downward wave are calculated to be about 4.9 h and 1284 km,

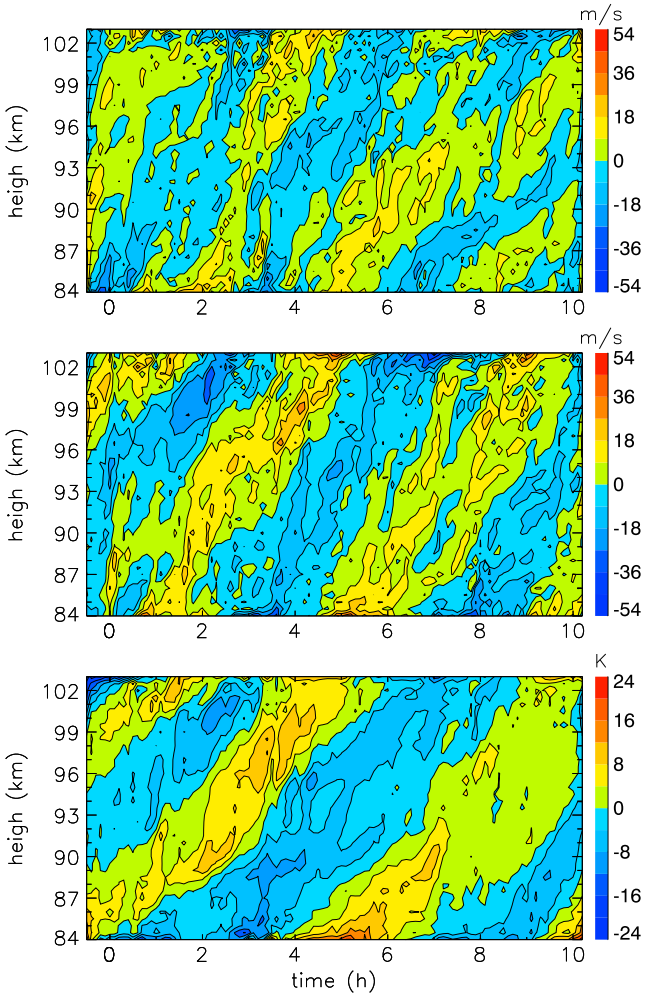

Figure 9. Downward propagating waves in (top) zonal wind, (middle) meridional wind, and (bottom) temperature.

respectively. Accordingly, the intrinsic horizontal and vertical group velocities are 69 ms^{-1} and 1.1 ms^{-1}. On the other hand, the horizontal kinetic energy and potential energy averaged in the height range of 84–103 km are about 27.8 Jkg^{-1} and 25.7 Jkg^{-1}, respectively. The intrinsic period is calculated to be 5.4 h, which is slightly larger than the value of 4.9 h derived from equations (3) and (4).

4. Discussion

In general, low-frequency IGWs have much larger horizontal wavelengths than high-frequency GWs. Since the ratio of horizontal-to-vertical group velocities for IGWs approximately equals the ratio of their horizontal-to-vertical wavelengths [*Fritts and Alexander*, 2003], IGWs propagate almost horizontally. For example, the upward and downward propagating waves in our study propagate with an elevation and depression angles of about 2.0° and 2.8°, respectively, in the absence of background wind. Consequently, when IGWs generated in the TLS propagate upward to the MLT, they must have travelled very long horizontal distances from their source region. At the same time, their propagation paths depend on the background conditions. The background wind velocity can directly add to the ground-based group velocity of wave, and the spatial and temporal variabilities of the background atmosphere can alter the intrinsic group velocities, and even the wave propagation direction [*Huang et al.*, 2008, 2010; *Snively*, 2013]. Here by means of wind data from HWM07 [*Drob et al.*, 2008] and temperature data from MSISE00 [*Picone et al.*, 2002], we perform a ray-tracing analysis to estimate the source region of the upward propagating IGW. The ray-tracing is done based on the equations of wave parameter evolution presented by *Yamamori and Sato* [2006]. The initial zonal and meridional wave numbers are $k_x = -2.6 \times 10^{-6}$ rad m^{-1} and $k_y = 6.2 \times 10^{-6}$ rad m^{-1} derived from its horizontal wave number $k_h = 6.7 \times 10^{-6}$ rad m^{-1} and its propagation direction of 337° azimuth; the initial vertical wave number is $k_z = 5.8 \times 10^{-4}$ rad m^{-1}; the initial longitude and latitude is 30.3°S, 70.7°W; the initial height is 90 km; and the beginning time is set to be 0500 UT, 21 July. The background information is obtained from HWM07 and MSISE00, and the inertia frequency and the Rossby parameter are determined by the latitude of wave position. The time step of numerical integration is taken to be 0.5 h, then the raypath is calculated by integrating backward in time. Figure 14 shows the raypaths in the longitude-height and longitude-latitude sections through the numerical integration for 37 h from 0500 UT, 21 July to 1600 UT, 19 July. The raypath is traced to be the height of 44.6 km over 62.2°S, 147.8°W after 37 h. Figure 15 presents the zonal wind over 62.2°S, 147.8°W at 1600 UT, 19 July. We can see from Figure 15 that there is an austral winter stratospheric jet with a maximum wind velocity of about 66 ms^{-1} at the height of around 37 km, and the wave locates in the jet region and is close to the jet center. Although we do not carefully

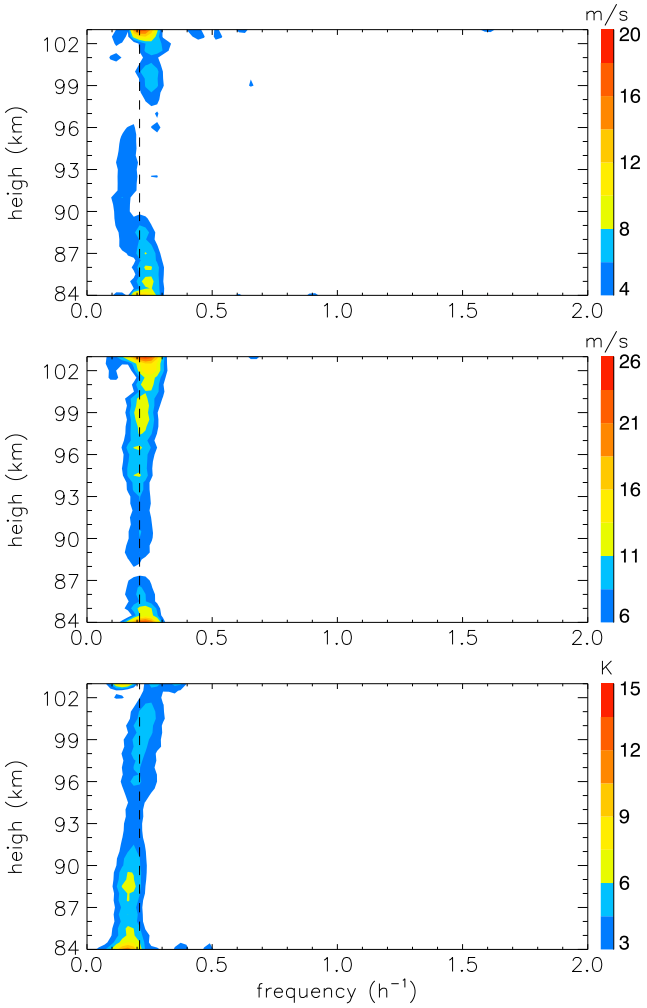

Figure 10. Lomb-Scargle frequency spectra of downward propagating waves in (top) zonal wind, (middle) meridional wind, and (bottom) temperature. The dashed vertical line corresponds to a period of 4.8 h.

compare the wave characteristics with the jet geostrophic adjustment processes, the 5.4 h upward propagating IGW is likely to come from the winter stratospheric jet region over the Antarctic because the wave has the typical time and space scales of IGWs radiated from the geostrophic adjustment [*Fritts and Alexander*, 2003]. Figure 16 presents the variation of intrinsic wave period with height and latitude. The intrinsic period is about 6.3 h at 1600 UT, 19 July, which approximately equals the 6 h period of the quarterdiurnal tide. Figure 16 illustrates that the intrinsic period exhibits an obvious variability with the background condition and inertia frequency alteration. This indicates that the wave is an IGW rather than a tidal component because as forced waves, the tides have only a very small change of period. A similar IGW which is possibly associated with the polar stratospheric jet adjustment is observed at the McMurdo station with an Fe lidar [*Chen et al.*, 2013].

A downward propagating IGW in the MLT is rarely reported. The clear upward phase progression shown in Figure 9 confirms that there existed a downward propagating IGW in the MLT on this night. In a realistic atmospheric wind field, a low-frequency GW may encounter a critical level, while a high-frequency GW is likely to encounter a reflection level [*Huang et al.*, 2010]. Even so, we may still evaluate whether or not the 4.8 h IGW is a result of an upward propagating IGW reflected from above. At the reflection level, the intrinsic frequency is Doppler-shifted to the buoyancy frequency. At this time, the vertical wave number becomes zero. By setting background temperature to be 1000 K in the thermosphere, the buoyancy frequency is calculated to be $N = 9.5 \times 10^{-3}$ rad s^{-1} and becomes larger if considering the positive temperature gradient in the thermosphere. According to equation (4), for the 4.8 h IGW with a horizontal wave number $k_h = 4.9 \times 10^{-6}$ rad m^{-1}, the wind velocity at the reflection level should be about 1860 ms^{-1} in the opposite direction of the wave propagation. When we further consider the positive temperature gradient due to the rapid increase of temperature with altitude in the lower thermosphere, the calculated buoyancy frequency is larger, which means that the reflection level requires a larger wind velocity. Such a large wind velocity is impossible in the realistic atmosphere so that the 4.8 h IGW is not likely from a reflection from above. This indicates that the source region of the downward propagating IGW is above the MLT. However, since we cannot estimate how long and how far the wave travels from its source region, we cannot conjecture the possible source region and the associated dynamical process of wave excitation yet.

For a medium-frequency GW propagating along a background wind shear, when the background wind velocity approaches the horizontal phase speed, the intrinsic frequency is close to zero due to the Doppler effect

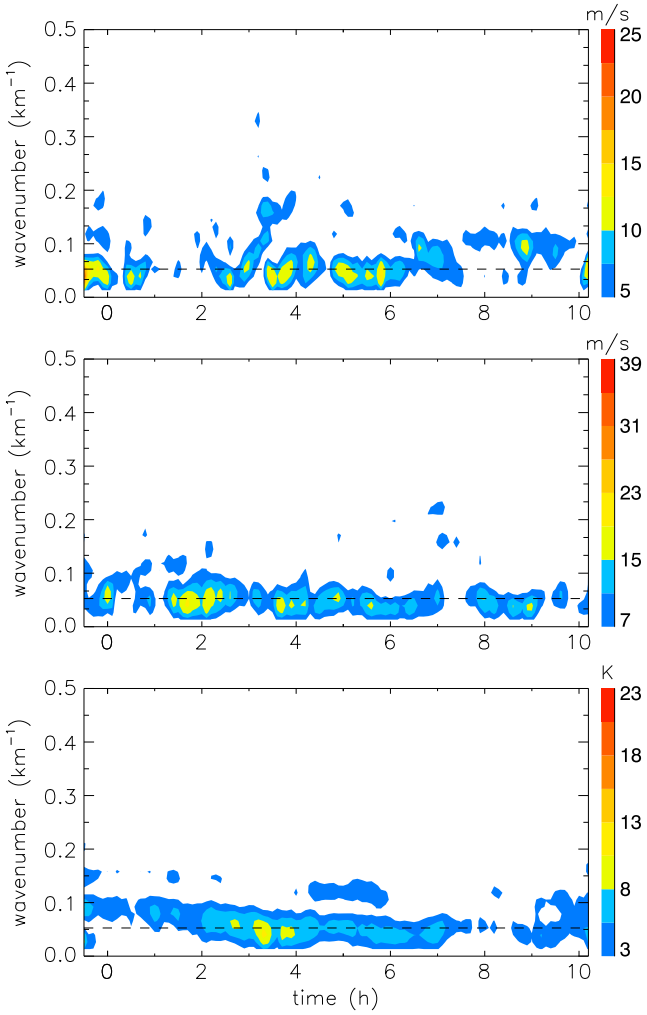

Figure 11. Lomb-Scargle wave number spectra of downward propagating waves in (top) zonal wind, (middle) meridional wind, and (bottom) temperature. The dashed horizontal line corresponds to a wavelength of 19 km.

and the vertical wave number approaches infinity. In this way, the wave encounters the critical level, which brings about the wave momentum deposition in the background flow due to the critical level absorption. However, for a low-frequency IGW, the intrinsic frequency at the critical level is nonzero and equal to the inertia frequency; thus, the wind velocity at the critical level is smaller than the horizontal phase speed [*Fritts and Alexander*, 2003]. Hence, it is possible for the IGWs to encounter the critical level when they propagate in the atmosphere. By taking $f = -7.4 \times 10^{-5}\,\mathrm{rad\,s^{-1}}$, the wind speeds at the critical level for the 5.4 h and 4.8 h IGWs are about $37.6\,\mathrm{ms^{-1}}$ and $59.9\,\mathrm{ms^{-1}}$ derived from equation (4), which are smaller than their horizontal phase speed of $48.6\,\mathrm{ms^{-1}}$ and $74.9\,\mathrm{ms^{-1}}$, respectively. Although the atmospheric zonal wind may be much larger than these speeds at the critical level, these two IGWs may propagate to the MLT without critical level filtering because their propagation directions are nearly in the meridional direction with about 20° departure rather than in the zonal direction.

According to the linear saturation theory of GWs [*Lindzen*, 1981; *Fritts*, 1984], once the GW amplitude exceeds the intrinsic horizontal phase speed, the wave becomes saturated and experiences severe dissipation due to dynamical and convective instabilities, which cause wave energy and momentum to be deposited into the background atmosphere. The maximum amplitude of the 5.4 h IGW in horizontal wind is $30.7\,\mathrm{ms^{-1}}$ at 96 km derived from the fitting, which is smaller than the intrinsic horizontal phase speed of $37.6\,\mathrm{ms^{-1}}$. Similarly, the maximum amplitude of $12.8\,\mathrm{ms^{-1}}$ at 94.5 km for the 4.8 h IGW is far smaller than the intrinsic horizontal phase speed of $72.2\,\mathrm{ms^{-1}}$. This indicates that as a single quasi-monochromatic wave, neither the 5.4 h nor the 4.8 h IGWs reach the amplitude threshold of instability. Nevertheless, the dynamical and convective instabilities may still take place due to superposition of different spectral components. Since the instabilities may arise from the effect of wave superposition, we use the wind and temperature in Figure 1 measured by lidar to calculate the Richardson number $Ri = \frac{N^2}{(\partial u/\partial z)^2 + (\partial v/\partial z)^2}$. Figure 17 depicts the Richardson number in the observational domain. Here we designate the dynamical instability area as where $0 < Ri < 0.25$ to distinguish it from the convective instability in which $N^2 < 0$. In Figure 17, the dynamical instability is denoted by light blue, while the convective instability is represented by dark blue. It can be seen from Figure 17 that the dynamical and convective instabilities occur discontinuously. By comparing Figure 17 with Figure 3, the downward evolution tendency of the unstable region is similar to the phase progression of the 5.4 h IGW, indicating that the 5.4 h IGW is the predominant perturbations, and the instability mainly arises from the superposition of other perturbations with the

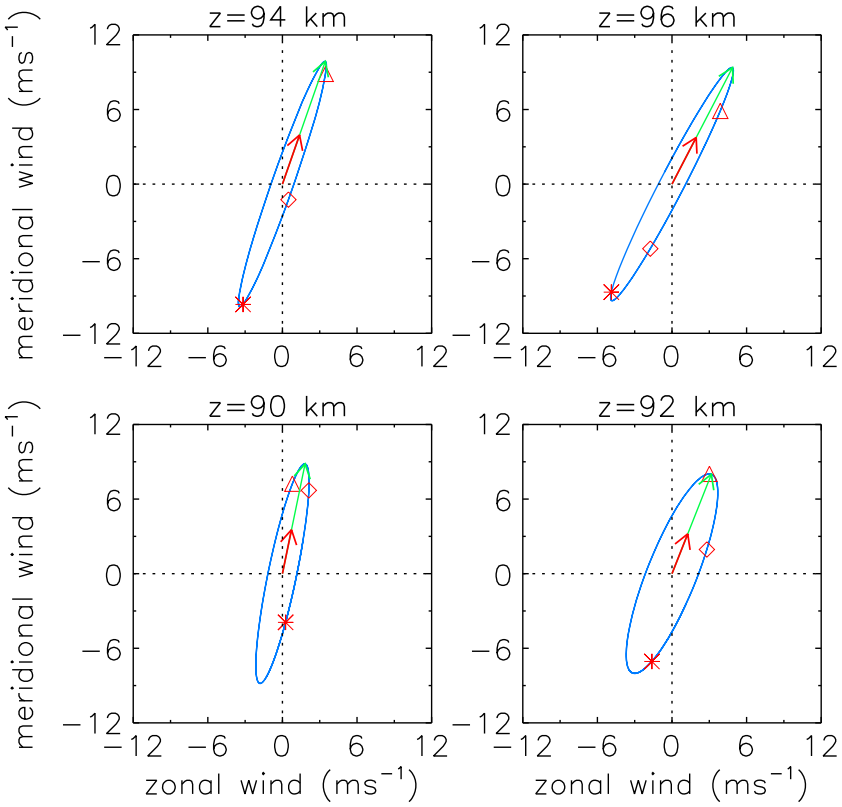

Figure 12. Temporal hodographs of zonal and meridional wind perturbations for 4.8 h wave. The star, square, and triangle are at 0, 1, and 2 h, respectively. The green arrow along the major axis of ellipse denotes the assumed propagation direction of the wave, and the red arrow denotes the realistic propagation direction.

5.4 h IGW. For a quasi-monochromatic wave, the occurrence of convective instability generally follows the dynamical instability [*Fritts and Isler*, 1994], while this scenario does not always occur for the superposition of multiple waves. In this way, the instability due to the superposition effect may play a significant role in wave amplitude constraint in the MLT since perturbations with different scales commonly overlap with each other in the atmosphere. At present, the effects of GW parameterization on the mean flow drag do not include this instability arising from the superposition; thus, a more sophisticated parameterization scheme of GWs should be developed to parameterize the saturation and instability of multiple-wave superposition.

5. Summary

In this paper, the IGW activities in the MLT are studied based on the ALO Na lidar observations from 2330 UT, 20 July to 1012 UT, 21 July 2015. An upward propagating IGW and a downward propagating IGW are simultaneously observed. The ground-based periods of the upward and downward propagating IGWs are about 5.4 h and 4.8 h, respectively. The maximum amplitude of the 5.4 h IGW is about 18.5 and 28.5 ms^{-1} in the zonal and meridional winds and 15.3 K in the temperature, respectively. In comparison, the 4.8 h IGW is weak. Both the spectral analysis and phase propagation indicate that the 5.4 h wave has a vertical wavelength of about 10.9 km. The vertical wavelength of the 4.8 h wave is about 22 km, derived from the phase evolutions. The hodographic technique is used to determine the horizontal propagation directions of the two IGWs. The 5.4 h IGW propagates in the direction of about 23° west of north, while the 4.8 h IGW propagates northward with an azimuth of about 20° clockwise from north.

We roughly estimate the intrinsic frequencies and horizontal wavelengths of these IGWs by combining the GW dispersion relation with the Doppler shift equation. The upward propagating IGW has a horizontal wavelength of 935 km. It propagates along the background wind of about 10.9 ms^{-1} in its horizontal propagation

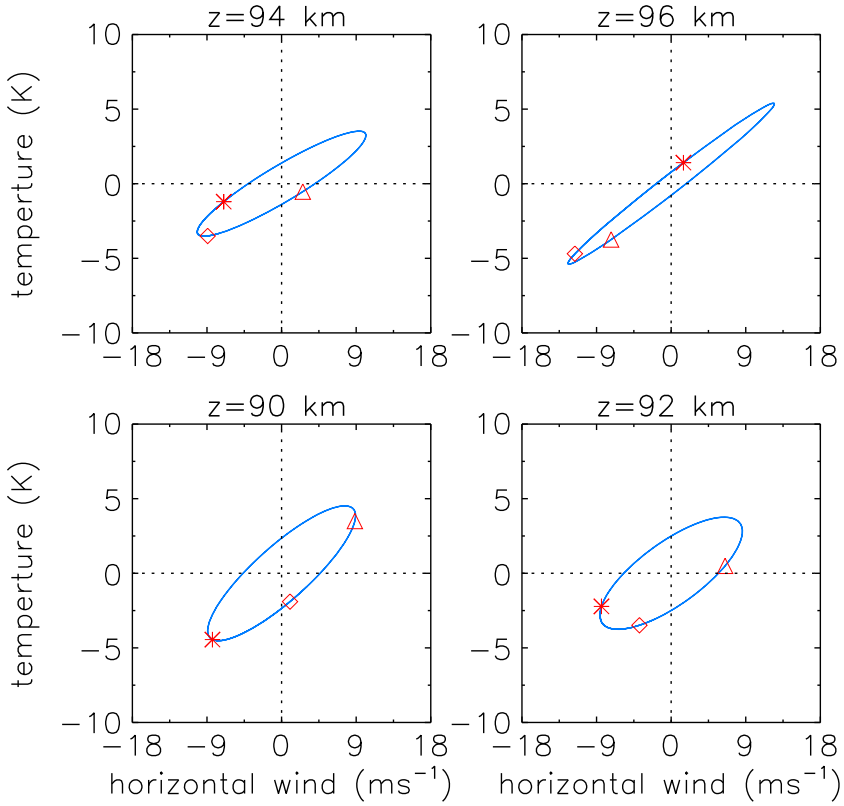

Figure 13. Temporal hodographs of temperature perturbation and horizontal wind perturbation in assumed propagation direction for 4.8 h wave. The star, square, and triangle are at 0, 1, and 2 h, respectively.

direction; thus, its intrinsic period of 6.9 h is larger than its ground-based period of 5.4 h. Its intrinsic horizontal and vertical group velocities are 34.5 ms^{-1} and 0.4 ms^{-1}, respectively. The horizontal wavelength of the downward propagating IGW is about 1248 km, and its intrinsic period of 4.9 h is slightly larger than the ground-based period of 4.8 h because it travels along the small background wind of 2.8 ms^{-1}. Its intrinsic horizontal and vertical group velocities are calculated to be 69 ms^{-1} and 1.1 ms^{-1}. Since the horizontal velocities of these waves are much larger than their vertical velocities, they propagate almost horizontally with very small elevation or depression angle of about 2–3°. These observed wave parameters are in the typical ranges presented in previous studies. Since many significant wave sources exist in the different atmospheric layers, the observational events of several dominating waves are a relatively common phenomenon. However, the downward propagating IGWs in the MLT are seldom reported in previous observations. Our observations indicate that there are downward propagating IGW activities in MLT.

With the help of data from HWM07 and MSISE00, the ray-tracing analysis indicates that the upward propagating IGW probably originates from the stratospheric unbalanced flow over the Antarctica. The downward propagating IGW is not likely to be a wave originated from the lower atmosphere and reflected above because a reflection level requires a very large unrealistic wind. We speculate that the wave may be generated above the MLT, but more work is needed to investigate this possibility.

The maximum horizontal wind amplitudes of 30.7 ms^{-1} and 12.8 ms^{-1} for the two IGWs are smaller than their intrinsic horizontal phase speeds of 37.6 ms^{-1} and 72.2 ms^{-1}, respectively. Thus, these IGWs do not reach the threshold of instability. However, the Richardson number and N^2 show the occurrence of dynamical and convective instabilities in some height and time due to the superposition of different perturbation components. Hence, the instability arising from the superposition effect may have a significant influence on wave saturation and amplitude constraint in the MLT. GW parameterizations do not include such effects, therefore may miss an important wave dissipation mechanism.

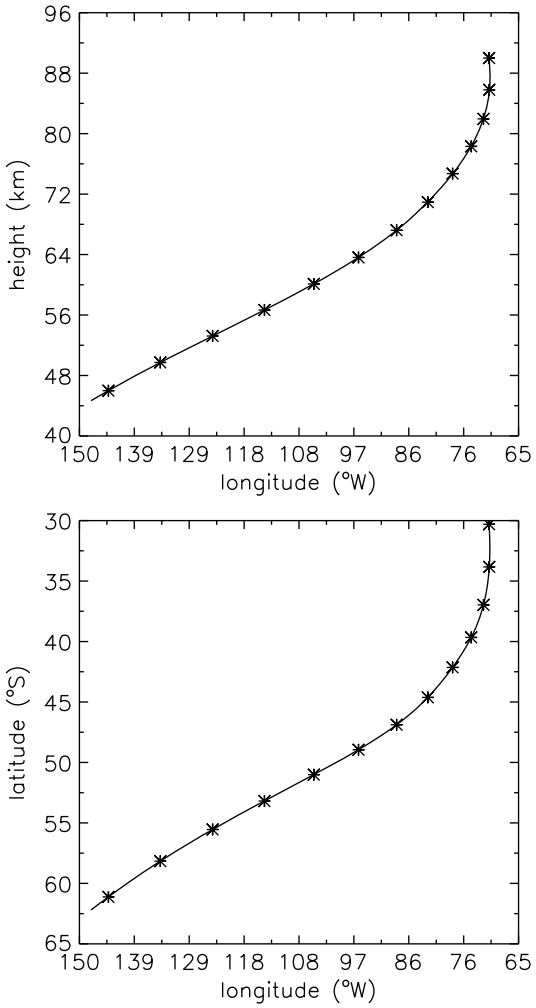

Figure 14. Ray paths in (top) longitude-height and (bottom) longitude-latitude sections by integrating backward in time for 37 h from 0500 UT, 21 July (30.3°S, 70.7°W) and the height of 90 km. The stars on the raypaths indicate the positions every 3 h from the starting point.

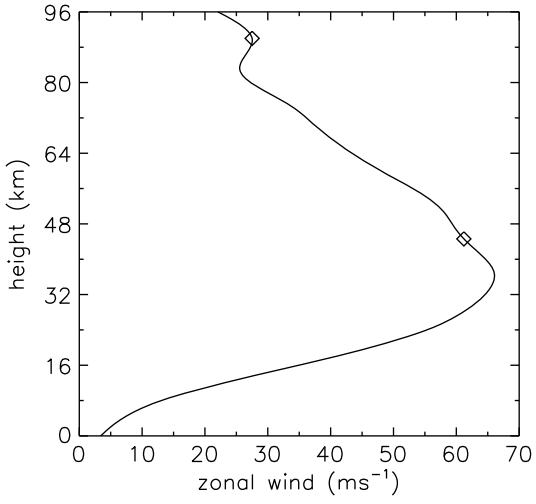

Figure 15. Zonal wind over (62.2°S, 147.8°W) at 1600 UT, 19 July. The two squares indicate the initial and final heights of integration, respectively.

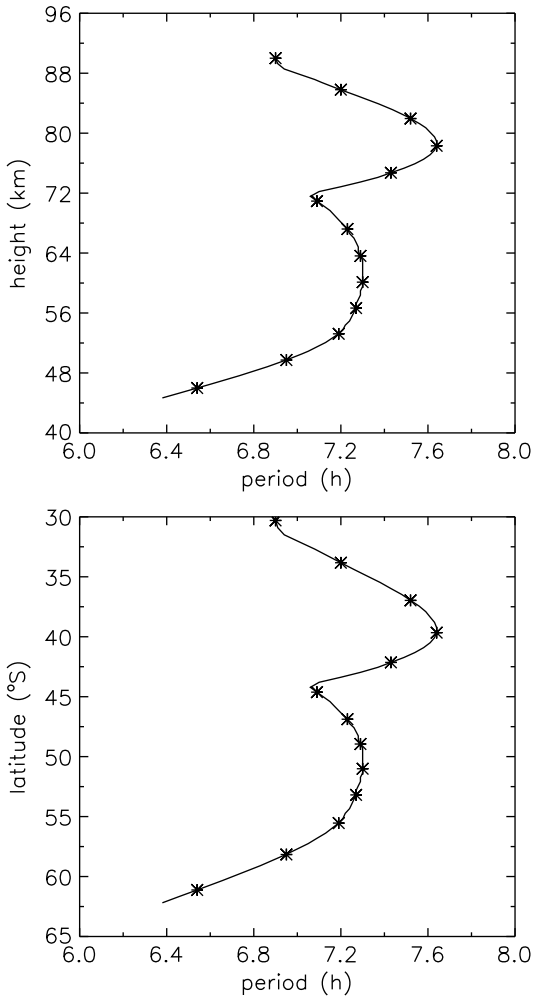

Figure 16. Evolution of intrinsic period with (top) height and (bottom) latitude. The stars indicate the period values every 3 h from the start.

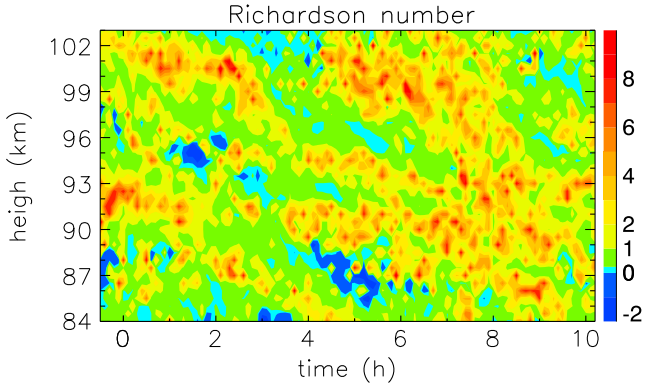

Figure 17. Richardson number. Note that the dynamical ($0 < Ri < 0.25$) and convective ($Ri < 0$) instabilities are denoted by light and dark blues, respectively.

Acknowledgments

We thank the editor and anonymous reviewers for their valuable comments on our paper. This work was jointly supported by the National Natural Science Foundation of China (through grants 41474127, 41674151, 41531070, and 41521063), the National Basic Research Program of China (grant 2012CB825605), the Specialized Fund for Comprehensive Study and Evaluation of the Polar Environment (grant CHINARE2016-0203), and the Open Programmes of Key Laboratory of Geospace Environment, CAS. The lidar data of this study are available at the Andes Lidar Observatory database at http:// lidar.erau.edu/data/.

References

Baumgarten, G., J. Fiedler, J. Hildebrand, and F.-J. Lübken (2015), Inertia gravity wave in the stratosphere and mesosphere observed by Doppler wind and temperature lidar, *Geophys. Res. Lett.*, *42*, 10,929–10,936, doi:10.1002/2015GL066991.

Cai, X., T. Yuan, Y. Zhao, P. D. Pautet, M. J. Taylor, and W. R. Pendleton Jr. (2014), A coordinated investigation of the gravity wave breaking and the associated dynamical instability by a Na lidar and an Advanced Mesosphere Temperature Mapper over Logan, UT (41.7°N, 111.8°W), *J. Geophys. Res. Space Physics*, *119*, 6852–6864, doi:10.1002/2014JA020131.

Chen, C., X. Chu, A. J. McDonald, S. L. Vadas, Z. Yu, W. Fong, and X. Lu (2013), Inertia-gravity waves in Antarctica: A case study using simultaneous lidar and radar measurements at McMurdo/Scott Base (77.8°S, 166.7°E), *J. Geophys. Res. Atmos.*, *118*, 2794–2808, doi:10.1002/jgrd.50318.

Chen, C., X. Chu, J. Zhao, B. R. Roberts, Z. Yu, W. Fong, X. Lu, and J. A. Smith (2016), Lidar observations of persistent gravity waves with periods of 3–10 h in the Antarctic middle and upper atmosphere at McMurdo (77.83°S, 166.67°E), *J. Geophys. Res. Space Physics*, *121*, 1483–1502, doi:10.1002/2015JA022127.

Chen, G., Z. Zhao, Y. Zhang, G. Yang, C. Zhou, S. Huang, T. Li, N. Li, and H. Sun (2011), Gravity waves and spread Es observed during the solar eclipse of 22 July 2009, *J. Geophys. Res.*, *116*, A09314, doi:10.1029/2011JA016720.

Chen, G., C. Wu, Z. Zhao, D. Zhong, H. Qi, and H. Jin (2014), Daytime E region field-aligned irregularities observed during a solar eclipse, *J. Geophys. Res. Space Physics*, *119*, 10,633–10,640, doi:10.1002/2014JA020666.

Chen, G., C. Wu, X. Huang, Z. Zhao, D. Zhong, H. Qi, L. Huang, L. Qiao, and J. Wang (2015), Plasma flux and gravity waves in the midlatitude ionosphere during the solar eclipse of 20 May 2012, *J. Geophys. Res. Space Physics*, *120*, 3009–3020, doi:10.1002/2014JA020849.

Cho, J. Y. N. (1995), Inertio-gravity wave parameter estimation from cross-spectral analysis, *J. Geophys. Res.*, *100*(D9), 18,727–18,737, doi:10.1029/95JD01752.

Collins, R. L., A. Nomura, and C. S. Gardner (1994), Gravity waves in the upper mesosphere over Antarctica: Lidar observations at the South Pole and Syowa, *J. Geophys. Res.*, *99*(D3), 5475–5485, doi:10.1029/93JD03276.

Drob, D. P., et al. (2008), An empirical model of the Earth's horizontal wind fields: HWM07, *J. Geophys. Res.*, *113*, A12304, doi:10.1029/2008JA013668.

Dunkerton, T. J. (1997), The role of gravity-waves in the quasi-biennial oscillation, *J. Geophys. Res.*, *102*(D22), 26,053–26,076, doi:10.1029/96JD02999.

Eckermann, S. D., I. Hirota, and W. K. Hocking (1994), Gravity wave and equatorial wave morphology of the stratosphere derived from long-term rocket sounding, *Q. J. R. Meteorol. Soc.*, *121*, 149–186.

Fritts, D. C. (1984), Gravity waves saturation in the middle atmosphere: A review of theory and observations, *Rev. Geophys.*, *22*, 275–308, doi:10.1029/RG022i003p00275.

Fritts, D. C., and M. J. Alexander (2003), Gravity wave dynamics and effects in the middle atmosphere, *Rev. Geophys.*, *41*(1), 1003, doi:10.1029/2001RG000106.

Fritts, D. C., and J. R. Isler (1994), Gravity wave breaking in two and dimensions, 2. Three-dimensional evolution and instability structure, *J. Geophys. Res.*, *99*, 8109–8123, doi:10.1029/93JD03436.

Fritts, D. C., S. L. Vadas, and Y. Yamada (2002), An estimate of strong local body forcing and gravity wave radiation based on OH airglow and meteor radar observations, *Geophs. Res. Lett.*, *29*(10), 1429, doi:10.1029/2001GL013753.

Gavrilov, N. M., S. Fukao, and T. Nakamura (2000), Average statistical characteristics of long gravity waves observed with the middle and upper atmosphere radar in the mesosphere, *J. Geophys. Res.*, *105*(D7), 9365–9379, doi:10.1029/1999JD901092.

Geller, M. A., and J. Gong (2010), Gravity wave kinetic, potential, and vertical fluctuation energies as indicators of different frequency gravity waves, *J. Geophys. Res.*, *115*, D11111, doi:10.1029/2009JD012266.

Hamilton, K. (1991), Climatological statistics of stratospheric inertia-gravity waves deduced from historical rocketsonde wind and temperature data, *J. Geophys. Res.*, *96*(D11), 20,831–20,839, doi:10.1029/91JD02188.

Holton, J. R. (2004), *An Introduction to Dynamic Meteorology*, Academic Press, London.

Hu, X., A. Z. Liu, C. S. Gardner, and G. R. Swenson (2002), Characteristics of quasi-monochromatic gravity waves observed with Na lidar in the mesopause region at Starfire Optical Range, NM, *Geophys. Res. Lett.*, *29*(24), 2169, doi:10.1029/2002GL014975.

Huang, K. M., and S. D. Zhang (2006), Numerical study on the propagation of gravity wave packet in time-variant background fields, *Chin. J. Space Sci.*, *26*(1), 35–42.

Huang, K. M., S. D. Zhang, and F. Yi (2008), Propagation and reflection of gravity waves in a meridionally sheared wind field, *J. Geophys. Res.*, *113*, D09106, doi:10.1029/2007JD008877.

Huang, K. M., S. D. Zhang, and F. Yi (2009), Gravity wave excitation through resonant interaction in a compressible atmosphere, *Geophys. Res. Lett.*, *36*, L01803, doi:10.1029/2008GL035575.

Huang, K. M., S. D. Zhang, and F. Yi (2010), Reflection and transmission of atmospheric gravity waves in a stably sheared horizontal wind field, *J. Geophys. Res.*, *115*, D16103, doi:10.1029/2009JD012687.

Huang, K. M., S. D. Zhang, F. Yi, C. M. Huang, Q. Gan, Y. Gong, and Y. H. Zhang (2013), Third-order resonant interaction of atmospheric gravity waves, *J. Geophys. Res. Atmos.*, *118*, 2197–2206, doi:10.1002/jgrd.50252.

Ki, M.-O., and H.-Y. Chun (2011), Inertia gravity waves associated with deep convection observed during the summers of 2005 and 2007 in Korea, *J. Geophys. Res.*, *116*, D16122, doi:10.1029/2011JD015684.

Krueger, D. A., C.-Y. She, and T. Yuan (2015), Retrieving mesopause temperature and line-of-sight wind from full-diurnal-cycle Na lidar observations, *Appl. Opt.*, *54*(32), 9469–9489.

Kumar, K. N., and T. K. Ramkumar (2008), Characteristics of inertia-gravity waves over Gadanki during the passage of a deep depression over the Bay of Bengal, *Geophys. Res. Lett.*, *35*, L13804, doi:10.1029/2008GL033937.

Li, T., C.-Y. She, H.-L. Liu, T. Leblanc, and I. S. McDermid (2007), Sodium lidar-observed strong inertia-gravity wave activities in the mesopause region over Fort Collins, Colorado (41°N, 105°W), *J. Geophys. Res.*, *112*, D22104, doi:10.1029/2007JD008681.

Li, T., T. Leblanc, I. S. McDermid, D. L. Wu, X. Dou, and S. Wang (2010), Seasonal and inter-annual variability of gravity wave activity revealed by long-term lidar observations over Mauna Loa Observatory, Hawaii, *J. Geophys. Res.*, *115*, D13103, doi:10.1029/2009JD013586.

Lindzen, R. S. (1981), Turbulence and stress owing gravity wave and tidal breakdown, *J. Geophys. Res.*, *86*, 9707–9714, doi:10.1029/JC086iC10p09707.

Liu, A. Z., Y. Guo, F. Vargas, and G. R. Swenson (2016), First measurement of horizontal wind and temperature in the lower thermosphere (105–140 km) with a Na Lidar at Andes Lidar Observatory, *Geophys. Res. Lett.*, *43*, 2374–2380, doi:10.1002/2016GL068461.

Liu, H.-L., and J. W. Meriwether (2004), Analysis of a temperature inversion event in the lower mesosphere, *J. Geophys. Res.*, *109*, D02S07, doi:10.1029/2002JD003026.

Lu, X., A. Z. Liu, G. R. Swenson, T. Li, T. Leblanc, and I. S. McDermid (2009), Gravity wave propagation and dissipation from the stratosphere to the lower thermosphere, *J. Geophys. Res.*, *114*, D11101, doi:10.1029/2008JD010112.

Lu, X., X. Chu, W. Fong, C. Chen, Z. Yu, B. R. Roberts, and A. J. McDonald (2015a), Vertical evolution of potential energy density and vertical wave number spectrum of Antarctic gravity waves from 35 to 105 km at McMurdo (77.8°S, 166.7°E), *J. Geophys. Res. Atmos.*, *120*, 2719–2737, doi:10.1002/2014JD022751.

Lu, X., C. Chen, W. Huang, J. A. Smith, X. Chu, T. Yuan, P. D. Pautet, M. J. Taylor, J. Gong, and C. Y. Cullens (2015b), A coordinated study of 1 h mesoscale gravity waves propagating from Logan to Boulder with CRRL Na Doppler lidars and temperature mapper, *J. Geophys. Res. Atmos.*, *120*, 10,006–10,021, doi:10.1002/2015JD023604.

Lu, X., X. Chu, H. Li, C. Chen, J. Smith, and S. Vadas (2017), Statistical characterization of high-to-medium frequency mesoscale gravity waves by lidar-measured vertical winds and temperatures in the MLT, *J. Atmos. Sol. Terr. Phys.*, doi:10.1016/j.jastp.2016.10.009, in press.

Moffat-Griffin, T., M. J. Jarvis, S. R. Colwell, A. J. Kavanagh, G. L. Manney, and W. H. Daffer (2013), Seasonal variations in lower stratospheric gravity wave energy above the Falkland Islands, *J. Geophys. Res. Atmos.*, *118*, 10,861–10,869, doi:10.1002/jgrd.50859.

Muraoka, Y., K. Kawahira, T. Sato, T. Tsuda, S. Fukao, and S. Kato (1987), Characteristics of mesospheric internal gravity waves observed by MU radar, *Geophys. Res. Lett.*, *14*(D11), 1154–1157, doi:10.1029/GL014i011p01154.

Murphy, D. J., S. P. Alexander, A. R. Klekociuk, P. T. Love, and R. A. Vincent (2014), Radiosonde observations of gravity waves in the lower stratosphere over Davis, Antarctica, *J. Geophys. Res. Atmos.*, *119*, 11,973–11,996, doi:10.1002/2014JD022448.

Nastrom, G. D., and F. D. Eaton (2006), Quasi-monochromatic inertia gravity waves in the lower stratosphere from MST radar observations, *J. Geophys. Res.*, *111*, D19103, doi:10.1029/2006JD007335.

Nicolls, M. J., R. H. Varney, S. L. Vadas, P. A. Stamus, C. J. Heinselman, R. B. Cosgrove, and M. C. Kelley (2010), Influence of an inertia-gravity wave on mesospheric dynamics: A case study with the Poker Flat Incoherent Scatter Radar, *J. Geophys. Res.*, *115*, D00N02, doi:10.1029/2010JD014042.

Pautet, P. D., M. J. Taylor, D. C. Fritts, K. Bossert, B. P. Williams, D. Broutman, J. Ma, S. D. Eckermann, and J. D. Doyle (2016), Large-amplitude mesospheric response to an orographic wave generated over the Southern Ocean Auckland Islands (50.7°S) during the DEEPWAVE project, *J. Geophys. Res. Atmos.*, *121*, 1431–1441, doi:10.1002/2015JD024336.

Pfenninger, M. A., A. Z. Liu, G. C. Papen, and C. S. Gardner (1999), Gravity wave characteristics in the lower atmosphere at South Pole, *J. Geophys. Res.*, *104*, 5963–5984, doi:10.1029/98JD02705.

Picone, J. M., A. E. Hedin, D. P. Drob, and A. C. Aikin (2002), NRLMSISE-00 empirical model of the atmosphere: Statistical comparisons and scientific issues, *J. Geophys. Res.*, *107*(A12), 1468, doi:10.1029/2002JA009430.

Rajeev, K., K. Parameswaran, M. N. Sasi, G. Ramkumar, and B. V. Krishna Murthy (2003), Rayleigh lidar observations of quasi-sinusoidal waves in the tropical middle atmosphere, *J. Geophys. Res.*, *108*(D24), 4749, doi:10.1029/2003JD003682.

Ratnam, V. M., A. N. Babu, V. V. M. J. Rao, S. V. B. Rao, and D. N. Rao (2008), MST radar and radiosonde observations of inertia-gravity wave climatology over tropical stations: Source mechanisms, *J. Geophys. Res.*, *113*, D07109, doi:10.1029/2007JD008986.

Riggin, D. M., D. C. Fritts, C. D. Fawcett, and E. Kudeki (1995), Observations of inertia-gravity wave motions in the stratosphere over Jicamarca, Peru, *Geophys. Res. Lett.*, *22*, 3239–3242, doi:10.1029/95GL03085.

Riggin, D. M., D. C. Fritts, C. D. Fawcett, E. Kudeki, and M. H. Hitchman (1997), Radar observations of gravity waves over Jicamarca, Peru during the CADRE campaign, *J. Geophys. Res.*, *102*, 26,263–26,281, doi:10.1029/96JD03675.

Sassi, F., and R. R. Garcia (1997), The role of equatorial waves forced by convection in the tropical semiannual oscillation, *J. Atmos. Sci.*, *54*, 1925–1942.

Sato, K., D. J. O'Sullivan, and T. J. Dunkerton (1997), Low-frequency inertia-gravity waves in the stratosphere revealed by three-week continuous observation with the MU radar, *Geophys. Res. Lett.*, *24*, 1739–1742, doi:10.1029/97GL01759.

Scargle, J. D. (1982), Studies in astronomical time series analysis, II. Statistical aspects of spectral analysis of unevenly spaced data, *Astrophys. J.*, *263*, 835–853.

She, C. Y., and J. R. Yu (1994), Simultaneous three-frequency Na lidar measurements of radial wind and temperature in the mesopause region, *Geophys. Res. Lett.*, *21*(17), 1771–1774, doi:10.1029/94GL01417.

Shimizu, A., and T. Tsuda (1997), Characteristics of Kelvin waves and gravity waves observed with radiosondes over Indonesia, *J. Geophys. Res.*, *102*, 26,159–26,171, doi:10.1029/96JD03146.

Smith, J. A., and X. Chu (2015), High-efficiency receiver architecture for resonance-fluorescence and Doppler lidars, *Appl. Opt.*, *54*(11), 3173–3184.

Snively, J. B. (2013), Mesospheric hydroxyl airglow signatures of acoustic and gravity waves generated by transient tropospheric forcing, *Geophys. Res. Lett.*, *40*, 4533–4537, doi:10.1002/grl.50886.

Sofko, G. J., and C. S. Huang (2000), SuperDARN observations of medium-scale gravity wave pairs generated by Joule heating in the auroral zone, *Geophys. Res. Lett.*, *27*, 485–488, doi:10.1029/1999GL003692.

Suzuki, H., T. Nakamura, S. L. Vadas, M. Tsutsumi, and M. Taguchi (2013), Inertia-gravity wave in the polar mesopause region inferred from successive images of a meteor train, *J. Geophys. Res. Atmos.*, *118*, 3047–3052, doi:10.1002/jgrd.50228.

Tsuda, T., Y. Murayama, H. Wiryosumarto, S. W. B. Harijono, and S. Sato (1994), Radiosonde observations of equatorial atmosphere dynamics over Indonesia: 2. Characteristics of gravity waves, *J. Geophys. Res.*, *99*, 10,491–10,506, doi:10.1029/94JD00355.

Vadas, S. L., D. C. Fritts, and M. J. Alexander (2003), Mechanism for the generation of secondary waves in wave breaking regions, *J. Atmos. Sci.*, *60*, 194–214.

Vincent, R. A., and M. J. Alexander (2000), Gravity waves in the tropical lower stratosphere: An observational study of seasonal and interannual variability, *J. Geophys. Res.*, *105*, 17,971–17,982, doi:10.1029/2000JD900196.

Vincent, R. A., A. Hertzog, G. Boccara, and F. Vial (2007), Quasi-Lagrangian superpressure balloon measurements of gravity-wave momentum fluxes in the polar stratosphere of both hemispheres, *Geophys. Res. Lett.*, *34*, L19804, doi:10.1029/2007GL031072.

Wilde, D. E. G., R. A. Vincent, C. Souprayen, S. Godin, A. Hertzog, and S. D. Eckermann (1997), Dual lidar observations of mesoscale fluctuations of ozone and horizontal winds, *Geophys. Res. Lett.*, *24*, 1627–1630, doi:10.1029/97GL01609.

Xu, J., A. K. Smith, R. L. Collins, and C. She (2006), Signature of an overturning gravity wave in the mesospheric sodium layer: Comparison of a nonlinear photochemical-dynamical model and lidar observations, *J. Geophys. Res.*, *111*, D17301, doi:10.1029/2005JD006749.

Yamamori, M., and K. Sato (2006), Characteristics of inertia gravity waves over the South Pacific as revealed by radiosonde observations, *J. Geophys. Res.*, *111*, D16110, doi:10.1029/2005JD006861.

Yamamoto, M., T. Tsuda, S. Kato, T. Sato, and S. Fukao (1987), A saturated internal gravity waves in the mesosphere observed by the middle and upper atmosphere radar, *J. Geophys. Res.*, *92*(D10), 11,993–11,999, doi:10.1029/JD092iD10p11993.

Yeh, K. C., and C. H. Liu (1974), Acoustic-gravity waves in the upper atmosphere, *Rev. Geophys.*, *12*, 193–216, doi:10.1029/RG012i002p00193.

Yoshiki, M., N. Kizu, and K. Sato (2004), Energy enhancements of gravity waves in the Antarctic lower stratosphere associated with variations in the polar vortex and tropospheric disturbances, *J. Geophys. Res.*, *109*, D23104, doi:10.1029/2004JD004870.

Yuan, T., et al. (2016), Evidence of dispersion and refraction of a spectrally broad gravity wave packet in the mesopause region observed by the Na lidar and Mesospheric Temperature Mapper above Logan, Utah, *J. Geophys. Res. Atmos.*, *121*, 579–594, doi:10.1002/2015JD023685.

Zhang, F., S. Wang, and R. Plougonven (2004), Uncertainties in using the hodograph method to retrieve gravity wave characteristics from individual soundings, *Geophys. Res. Lett.*, *31*, L11110, doi:10.1029/2004GL019841.

Zhang, S. D., and F. Yi (2005), A statistical study of gravity waves from radiosonde observations at Wuhan (30°N, 114°E), China, *Ann. Geophys.*, *23*, 665–673.

Zhang, S. D., and F. Yi (2007), Latitudinal and seasonal variations of inertial gravity wave activity in the lower atmosphere over central China, *J. Geophys. Res.*, *112*, D05109, doi:10.1029/2006JD007487.

Zhou, Q., and Y. T. Morton (2006), A case study of mesospheric gravity wave momentum flux and dynamical instability using the Arecibo dual beam incoherent scatter radar, *Geophys. Res. Lett.*, *33*, L10802, doi:10.1029/2005GL025608.

Zink, F., and R. A. Vincent (2001), Wavelet analysis of stratospheric gravity wave packets over Macquarie Island: 1. Wave parameters, *J. Geophys. Res.*, *106*, 10,275–10,288, doi:10.1029/2000JD900847.